JACS Au
AN OPEN ACCESS JOURNAL OF THE AMERICAN CHEMICAL SOCIETY

pubs.acs.org/jacsau
Article

Accelerated Selective Electrooxidation of Ethylene Glycol and Inhibition of C−C Dissociation Facilitated by Surficial Oxidation on Hollowed PtAg Nanostructures via In Situ Dynamic Evolution

Yuhan Li, Qingliang Liao, Peiyi Ji, Sheng Jie, Chunjie Wu, Kunyi Tong, Minghui Zhu, Chenhao Zhang,* and Hui Li*

Cite This: JACS Au 2025, 5, 714−726
Read Online

ACCESS | Metrics & More | Article Recommendations | Supporting Information

ABSTRACT: Electro-upgrading of low-cost alcohols such as ethylene glycol is a promising and sustainable approach for the production of value-added chemicals while substituting energy-consuming OER in water splitting. However, the sluggish kinetics and possibility of C−C dissociation make the design of selective and efficient electrocatalysts challenging. Herein, we demonstrate the synthesis of a hollowed bimetallic PtAg nanostructure through an in situ dynamic evolution method that could efficiently drive the selective electrochemical ethylene glycol oxidation reaction (EGOR). The resulting mild surficial oxidation has intrinsically improved EGOR activity, exhibiting a remarkable performance toward glycolate (selectivity up to 99.2% and faradic efficiency ~97%) at high current density with low overpotential (355 mA·cm^{-2} at 1.0 V, 16.3 A·mg$_{Pt}^{-1}$), exceeding prior outcomes. Through comprehensive operando characterization and theoretical calculations, this study systematically reveals that the in situ formation of Pt−O(H)$_{ad}$ is pivotal for modulating the electronic structure of surface and facilitating the selective electrooxidation and adsorption of −CH$_2$OH. The competitive C−C dissociation pathway toward HCOO$^-$ is concurrently inhibited in comparison to Pt. An industrial-level current coupled with hydrogen production at low cell voltages was also achieved. These findings offer more in-depth mechanistic understanding of the EGOR's reaction pathway mediated by surface environment in Pt-based electrocatalysts.

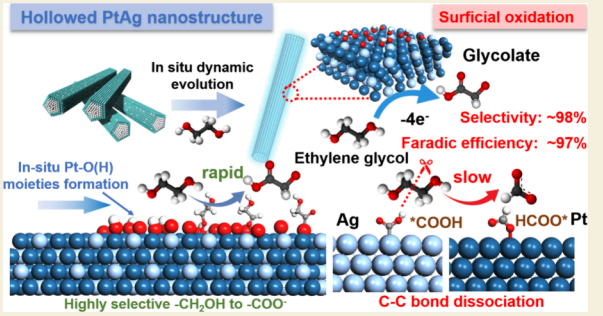

KEYWORDS: *selective electrochemical oxidation, ethylene glycol, surficial modulation, in situ characterization, glycolate*

INTRODUCTION

Electrochemical oxidation reactions have been regarded as an economic and environmentally friendly methodology for upgrading low-cost organic molecule precursors into various valuable chemicals, which also serve as an alternative to energy-consuming OER in water splitting.[1−5] As the smallest polyol, ethylene glycol (EG), readily acquired from the chemical industry or the degradation of polyethylene terephthalate (PET) plastic, could be considered a model reactant for the investigation of selective alcohol electrooxidation.[6−8] Furthermore, the electrooxidation of EG (~0.6 US$/kg) has been considered to be a promising route for the synthesis of glycolic acid or glycolate (~3.1 US$/kg) with a high economic benefit. Particularly within the past few years, glycolic acid has gained significant traction in the fabrication of biodegradable polymers including polyglycolide (PGA) and poly(lactic-*co*-glycolic acid) (PLGA), especially considering the remarkable degradation feasibility of these polymers relative to the traditional biodegrade plastics such as PLA.[9,10] In this context, the exploration of an efficient and high-performance electrooxidation approach for converting EG to glycolate is of significant interest.

Nonetheless, there are challenges associated with the selectivity of electrochemical reactions that often restrict the effectiveness of electrooxidation with alcohol.[11,12] For instance, the comprehensive electrooxidation pathway of EG is inherently complex, potentially involving up to 10 electrons per molecule. This process can occur through several consecutive and/or parallel proton-coupled electron transfer (PCET) steps, featuring various reaction intermediates such as glycolaldehyde, glyoxal, glycolic acid, glyoxylic acid, oxalic acid, formic acid, and final product CO_2.[13−18] Especially, the uncontrolled C−C bond dissociation during the electrooxidation process is one of the major side reactions to harness

Received: October 16, 2024
Revised: January 8, 2025
Accepted: January 9, 2025
Published: January 24, 2025

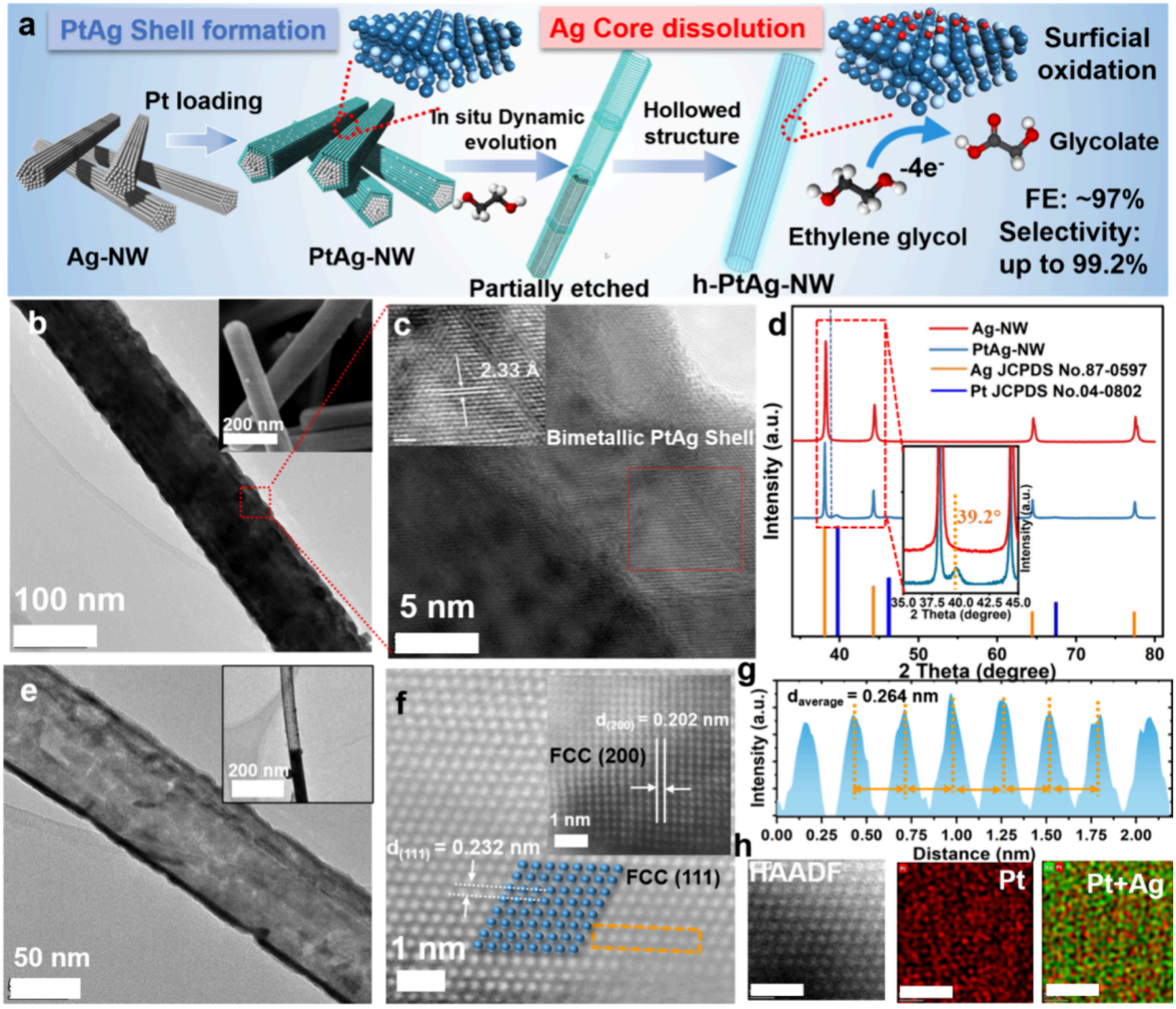

Figure 1. (a) Schematic illustration of the synthetic procedure of the Ag-NW, PtAg-NW, and corresponding in situ dynamic evolution toward the formation of h-PtAg-NW. (b) TEM and inset SEM images of the PtAg-NW. (c) High-resolution TEM image of PtAg-NW at the intersection region between shell and core (inset: enlarged lattice fringes of PtAg shell). (d) XRD patterns of the Ag-NW and PtAg-NW, along with references. (e) Representative TEM images of the h-PtAg-NW and partially etched PtAg-NW (inset). (f) Aberration-corrected HAADF-STEM images for h-PtAg-NW (spheres represents Pt or Ag atoms) and FCC (111), (200) (inset) crystal plane spacing illustrated. (g) Line intensity profile acquired along the orange square in (f). (h) Local EDS mapping of the h-PtAg-NW with high magnification (scale bar 1 nm).

the selectivity of EG toward glycolic acid or glycolate, leading to the undesired C1 byproduct such as formate.[19−21] The catalytic sites' structure and reaction mechanism governing the selection between C−C bond dissociation and −OH electro-oxidation have not yet been fully elucidated. Therefore, achieving sufficient selectivity and obtaining the desired electro-oxidized products through the partial oxidation of EG under large current still remain a considerable obstacle.

With the aim of improving the product selectivity of EG electrooxidation, there is a growing need to design electro-catalysts with precise control over the oxidation pathway. The electrooxidation reaction should focus on the transformation of a single hydroxyl group to the carboxylic group, avoiding the cleavage of the C−C bond and other overoxidation reactions. Owing to the unique d-band electron structure and chemical stability, low-dimensional metal nanomaterials, particularly with Pd, Pt, Ru, and Au, are of great interest in electrocatalysis including electrooxidation reactions for organic molecules such as alcohols, aldehyde, and alkylene.[22−28] However, their high activity, which often leads to an induced C−C bond dissociation pathway, still imposes a great burden on the selective electrooxidation of EG. One critical factor ruling the performance of electrooxidation is the modulation of the catalytic surface of metallic nanomaterials during the reaction. Meanwhile, the large reaction current density will be essential for industrial and economic feasibility, which requires the optimization of both superior mass transportation and efficient catalytic sites. Referring to the recent reports, incorporating nanoscale interior cavities into metallic nanomaterials represents a novel and remarkably effective approach for increasing the surface area and creating diffusion channels for electrochemical reactions and other applications.[29−37] The hollowed nanostructure could also increase the atom-utilization efficiency of noble metals, alleviating the waste of submerged internal atoms. Of greater intrigue, the introduction of a nanocavity in metallic nanoparticles also has the capability

https://doi.org/10.1021/jacsau.4c00975
JACS Au 2025, 5, 714−726

to modulate their electronic and surficial structure. Moreover, these features offer meticulously controlled electronic structure and nanoscale environments, which could potentially be harnessed to fine-tune the electrocatalytic selectivity toward specific products, synergistically enhancing their catalytic performances.[38−43]

Herein, we first demonstrate that a hollowed PtAg nanostructure electrocatalyst (denoted as h-PtAg-NW) could be synthesized via an in situ dynamic electrochemical evolution method. Notably, the h-PtAg-NW exhibits exceptional activity for promoting the electrochemical EG oxidation reaction (EGOR) and its conversion to glycolate in an alkaline environment with superior selectivity (>98%). This is highlighted by the onset potential requirement of only 0.63 V versus RHE to achieve a current density of 100 mA cm^{-2}, and 1.0 V to deliver 355 mA cm^{-2} (mass activity of 16.3 A mg_{Pt}^{-1}) with glycolate selectivity up to 99.2%, which is the highest selectivity reported and surpasses most of the prior results. Furthermore, the catalyst demonstrates an industrial-level current of up to 1.0 A cm^{-2} coupled with hydrogen production in a flow cell assembly at low voltages, while attaining remarkable Faradaic efficiencies (>95%). Experimental evidence suggests that the electrochemical dissolution process exposes more surface areas and an intrinsically enhanced EGOR reactivity for h-PtAg-NW during the hollowed nanostructure formation. In situ Raman and FTIR characterizations further reveal that the appearance of Pt−OH_{ad} and Pt−O_{ad} (Pt−O(H)) moieties associated with high glycolate selectivity and no C1 species adsorbed on h-PtAg-NW. On the contrary, the HCOO* and *COOH intermediates are identified on metallic Pt and Ag surfaces, respectively, which are related with C−C dissociation and the generation of byproduct formate. Density functional theory (DFT) calculation also unveils that the electrooxidation of EG to glycolate is energetically and electronically structure-flavored on Pt_3Ag with mild surficial oxidation, while the competitive C−C dissociation pathway is suppressed, leading to its highly efficient and selective EGOR performance. These findings collectively demonstrate the significant advancements achieved with this Pt-based hollowed nanostructure through an in situ electrochemical process, and the importance of the surface environment in the domain of selective electrooxidation of alcohols and the associated applications.

RESULTS AND DISCUSSION

Synthesis of a Hollowed Bimetallic PtAg Nanostructure

The synthesis process of the hollowed bimetallic PtAg nanostructure (h-PtAg-NW) is outlined in Figure 1a. The Ag nanowire (Ag-NW) backbone was prepared through a solution-phase polyol method (details of the method in the Supporting Information).[44] The representative scanning electron microscopy (SEM) and transmission electron microscopy (TEM) images (Figure S1) indicate a typical morphology of the synthesized Ag-NW with an average diameter of ca. 100 nm and length up to several micrometers as well as expected (100) facet exposed through the lateral direction. The subsequent Pt deposition was accomplished through a hydrothermal reaction involving Ag-NW and a $Pt(acac)_2$ precursor, resulting in the formation of Pt-loaded Ag-NW nanowires (PtAg-NW). After Pt loading, the nanowire-like morphology of Ag-NW was well-preserved in PtAg-NW, as confirmed by the TEM and SEM characterizations with similar diameters and lengths (Figure 1b and Figure S2). High-resolution TEM (HRTEM) images of the outermost region of PtAg-NW reveal more structural insights into the deposition of Pt. As shown in Figure 1c, a shell-like structure with an average thickness of ca. 10 nm envelops the inner structure of the Ag nanowire. The enlarged inset image in Figure 1c demonstrates that the outermost crystalline structure possesses an interplanar spacing of 2.33 Å, which is intermediate between the lattice spacing of (111) planes in face-centered cubic (FCC) Pt (0.227 nm) and Ag (0.236 nm), suggesting alloying between Pt and Ag. The powder X-ray diffraction (XRD) pattern (Figure 1d) of Ag-NW indicates diffraction peaks at 38.1, 44.4, 64.6, and 77.5°, which correspond well to those of the FCC Ag (JCPDS No. 87-0597).[45] Meanwhile, for PtAg-NWs, the emergence of a new diffraction peak centering at 39.2° could be observed, further substantiating the successful deposition of metallic Pt alloy on PtAg-NW.[46] A series of control samples, denoted as Pt_xAg-NW, were synthesized with varying Pt loadings. The XRD diffraction peak at 39.2° progressively intensified with an increase in Pt loading (Figure S3). Reports suggest that the exterior metallic Ag on the Ag-NW can be partly substituted by Pt through a galvanic exchange reaction with the Pt precursor ($2Ag + Pt^{2+} \rightarrow 2Ag^{+} + Pt$), resulting in the formation of the intermetallic PtAg alloy shell (Figure S4).[47,48] To in situ modify the nanostructure of PtAg-NW and probe its EGOR activity, PtAg-NW was then loaded on the carbon paper (CP) electrode and underwent anodic electrochemical scanning with the presence of EG. Intriguingly, TEM characterization revealed a dynamic morphological and structural evolution of PtAg-NW. It was found that electrochemical oxidation treatment in EG could selectively dissolve away the Ag interior core while retaining the void PtAg shell framework. The representative TEM images of partially etched PtAg-NW (inset of Figure 1e) demonstrate a half-hollowed nanowire to nanotube morphology. As the gradual dissolution of the Ag inner structure continues, after 90 min of treatment with the positive potential of +1.4 vs RHE in 1 M KOH and 1.5 M EG aqueous electrolyte, the in situ dynamic etched hollowed PtAg nanostructure (h-PtAg-NW) was acquired with the outermost shell preserved (Figure 1e and Figure S5). The aberration-corrected high-angle annular dark-field scanning transmission electron microscopy (HAADF-STEM) of h-PtAg-NW was further probed to identify its atomic-level crystalline structure. Figure 1f displays a characteristic atomic resolution HAADF-STEM image of the shell layer in h-PtAg-NW. The lattice spacings of 0.232 and 0.202 nm are measured, corresponding to the (111) and (200) crystal planes in FCC-ordered PtAg alloy. The distance between metal atoms is 2.64 Å according to the line intensity profile, as depicted in Figure 1g, which falls within the range between the Pt−Pt bond (2.60 Å) and the Ag−Ag bond (2.68 Å). To further evaluate the elemental distribution of h-PtAg-NW, energy-dispersive spectroscopy (EDS) elemental mappings of the lattice region are shown in Figure 1h. It is noteworthy that in the local EDS mapping, not only the signal indicative of Pt was observed but also the uniform presence of Ag, confirming that the remaining shell for h-PtAg-NW is mainly composed of a bimetallic PtAg nanostructure.

Structural Characterization

To directly probe the dynamic evolution of nanostructures along with their elemental composition, EDS mapping was

https://doi.org/10.1021/jacsau.4c00975
JACS Au 2025, 5, 714−726

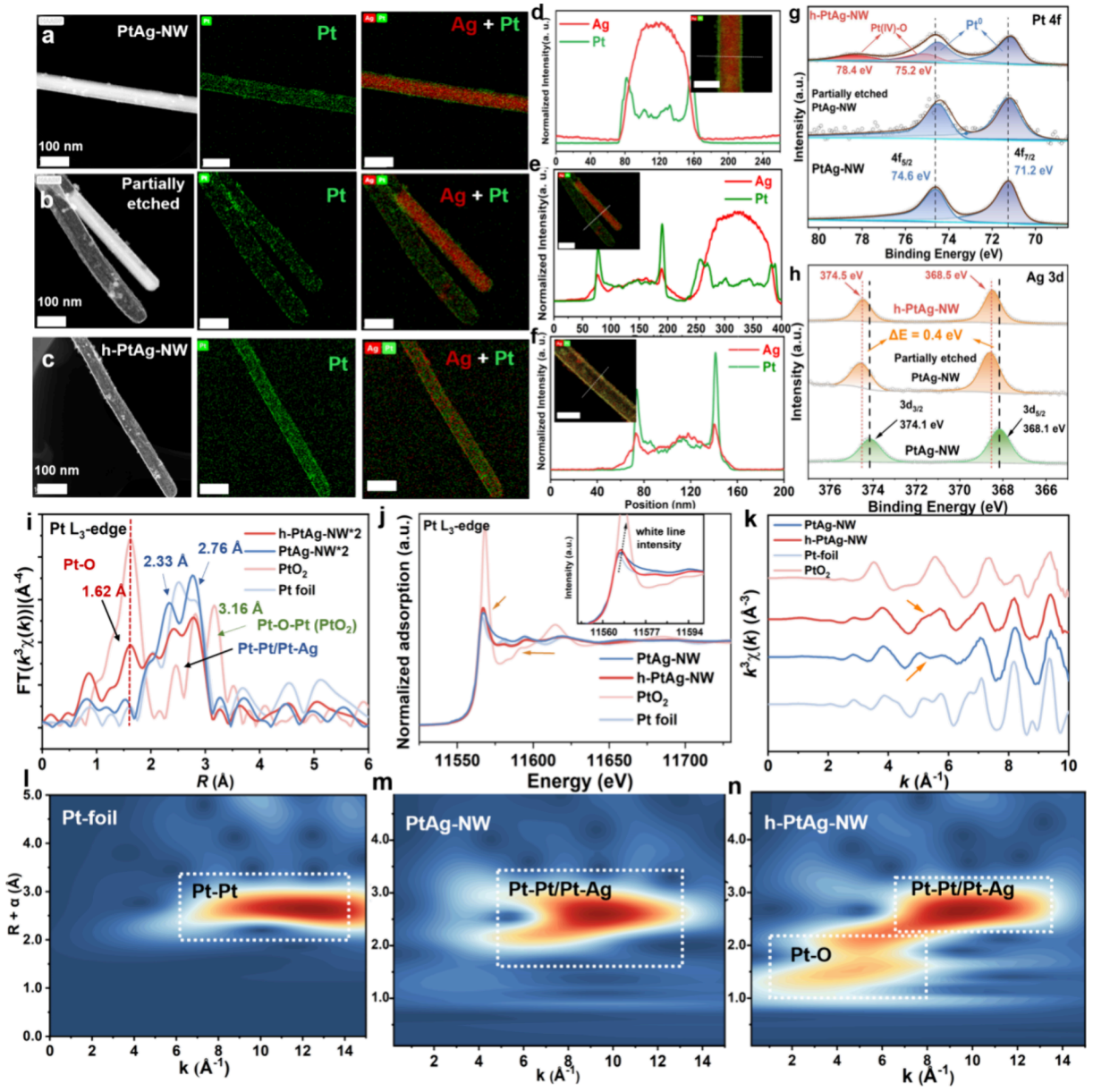

Figure 2. (a–c) HAADF-STEM images and EDS mapping of PtAg-NW (a), partially etched PtAg-NW (b), and h-PtAg-NW (c), respectively, with Ag (red) and Pt (green) elemental mapping. (d–f) EDS line-scanning profile of Ag and Pt along the direction shown in the inset mapping image (scale bar 100 nm) for PtAg-NW, partially etched PtAg-NW, and h-PtAg-NW. (g) Pt 4f and (h) Ag 3d XPS spectra of PtAg-NW, partially etched PtAg-NW, and h-PtAg-NW. (i) Fourier transform (FT) of the k^3-weighted EXAFS of PtAg-NW, h-PtAg-NW, and Pt foil, PtO_2 references. (j) Normalized XANES spectra in the Pt L_3-edge and enlarged edge region (the inset) of PtAg-NW, h-PtAg-NW, and Pt foil, PtO_2 references. The increase in white line intensity and adsorption features are labeled. (k) k^3-weighted Pt L_3-edge EXAFS oscillation curves of PtAg-NW, h-PtAg-NW, and Pt foil, PtO_2 references. (l–n) Wavelet transformation (WT) for the EXAFS spectra of Pt foil (l), PtAg-NW (m), and h-PtAg-NW (n). The highlighted region in the spectrum of h-PtAg-NW at 4.5 $Å^{-1}$ is associated with the Pt–O contribution.

further performed on PtAg-NW, partially etched PtAg-NW, and final h-PtAg-NW with distinct signals corresponding to Ag (red), Pt (green), and combined (Figure 2a–f). The outcomes confirmed the presence of a shell layer with Pt signals surrounding the Ag core (Figure 2a,d), further unveiling the homogeneous presence of Pt covering the surface of the nanowires. As the oxidation proceeds, certain Ag inner cores undergo oxidative dissolution with the presence of EG in the electrolyte, yielding Pt and Ag containing hollow tubular structures (Figure 2b and Figure S6). A portion of partially etched PtAg nanowires remained solid, exhibiting a unique structure comprising half-hollow tubes and half-solid segments, as demonstrated in the line-scanning profile in Figure 2e. Eventually, after deep electrooxidation, the nanostructure obtained after electrochemical treatment exhibited a hollow, slender nanotube morphology, as shown in Figure 2c. In the EDS mapping, most of the Ag interior has dissolved away, leaving behind a thin wall to support the hollowed nanostructure. Meanwhile, EDS results further revealed the presence of Ag and Pt signals in the walls of hollow nanotubes (Figure 2f), verifying that the shell layer consists of a bimetallic PtAg alloy formed via the galvanic exchange. Furthermore, it was identified by the EDS point analysis spectrum that the atomic ratio of Pt:Ag in the nanowire has drastically increased

https://doi.org/10.1021/jacsau.4c00975
JACS Au 2025, 5, 714–726

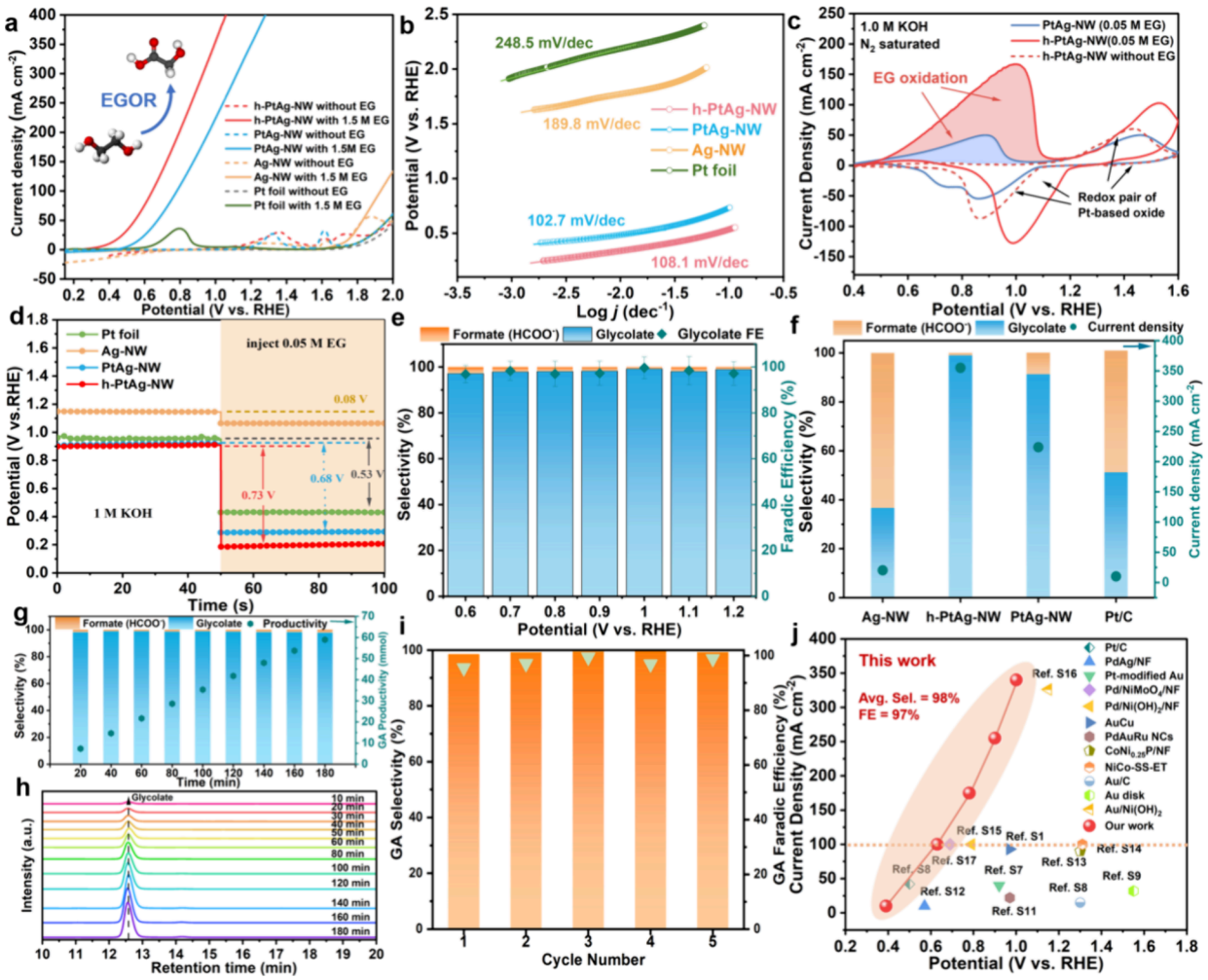

Figure 3. (a) LSV profiles of h-PtAg-NW, PtAg-NW, Pt foil, and Ag-NW with or without 1.5 M EG. (b) Tafel plots of EGOR with h-PtAg-NW, PtAg-NW catalyst, and Pt/C and Ag-NW references. (c) CV curves of h-PtAg-NW and PtAg-NW with or without 0.05 M EG. (d) OCPs of h-PtAg-NW, PtAg-NW, Pt foil, and Ag-NW in 1 M KOH before and after EG addition (e) Selectivity and Faradaic efficiency for glycolate and formate byproduct on h-PtAg-NW with different potentials (1.5 M EG and 1 M KOH). (f) Selectivity and current density with h-PtAg-NW, PtAg-NW, Pt/C, and Ag-NW. (g) Selectivity and productivity of glycolate with the h-PtAg-NW catalyst through chronoamperometry measurement at 1.0 V vs RHE. (h) HPLC chromatogram of electrolyte for product analysis. (i) Selectivity and faradic efficiency of glycolate (GA) on h-PtAg-NW of each cycle with 2 h electrolysis and activation. (j) Potential and corresponding current density diagram of our result in comparison with reported results for EGOR. The potentials at 100 mA cm^{-2} are highlighted by a dashed line.

from 1:7.1 to 1:1.2 in h-PtAg-NW (Figure S7), consistent with the dissolution of Ag. A control experiment was also conducted to investigate the dynamic evolution conditions and to further elucidate the role of EG. As illustrated in Figure S8, it was found that without the presence of EG, no apparent hollowed structures could be observed after the electrooxidation upon PtAg-NW. Moreover, the dissolution of Ag was quantified by means of the measurement of ICP-OES, and 10.08 μg/mL Ag was detected in the EG and KOH electrolyte after oxidative evolution toward h-PtAg-NW. In contrast, only 0.78 μg/mL Ag was detected in the KOH electrolyte without EG, which suggests that the electrochemical dissolution of Ag cores was possibly assisted by the presence of EG. The control experiments further demonstrated that ethanol could also induce the formation of hollowed nanostructures in contrast to methanol (Figure S9). The electrochemical dissolution of Ag cores is possibly promoted by the interaction or coordination between Ag^+ and carboxylate species generated during the electrochemical oxidation process.[49]

To unravel the mechanistic insight into this dynamic electrochemical evolution process, X-ray photoelectron spectroscopy (XPS) and X-ray absorption fine structure (XAFS) characterization were performed to probe the electronic states and chemical environment of PtAg nanostructures. The high-resolution XPS of Pt 4f in untreated PtAg-NW shows metallic Pt $4f_{5/2}$ and Pt $4f_{7/2}$ peaks with the binding energies of 74.6 and 71.2 eV (Figure 2g). After electrochemical oxidation, XPS analysis revealed that the signal of Pt species was shifted to a higher valence state with the appearance of Pt (IV) species in h-PtAg-NW catalysts. Meanwhile, the $3d_{5/2}$ and $3d_{3/2}$ signals of Ag also positively drifted toward a higher binding energy (ΔE = 0.4 eV) (Figure 2h). Intriguingly, considering the XPS spectrum of partially etched half-hollow PtAg-NW, the positive shifting of the Ag signal could be detected, while no significant shift was observed for the Pt signal. This phenomenon allows us to infer that the oxidative dissolution of Ag is the initial step in this process. At the end stage of complete transformation, the electrooxidation also occurred on the remaining PtAg shell, leading to the appearance of Pt moieties with higher valence.

https://doi.org/10.1021/jacsau.4c00975
JACS Au 2025, 5, 714−726

An enhanced signal for the h-PtAg-NW in electron paramagnetic resonance (EPR) was induced by polarized-spin alignment due to increased unpaired electrons after oxidation (Figure S10). In order to further elucidate the detailed information on the local coordination environments of the Pt shell layer in the h-PtAg-NW catalyst, extended X-ray absorption fine structure (EXAFS) and X-ray absorption near-edge structure (XANES) characterization at the Pt L_3-edge were performed. The Fourier-transformed (FT) k^3-weighted EXAFS oscillations of h-PtAg-NW, PtAg-NW, Pt foil, and PtO_2 references were analyzed and are shown in Figure 2i. The PtAg-NW shows a prominent peak at 2.76 Å and a shoulder peak at 2.33 Å in R-space, contributed by the combination of Pt−Pt and Pt−Ag scattering paths, respectively. In comparison, a weak peak emerged at 1.62 Å in h-PtAg-NW catalysts, possibly associated with the Pt−O bond according to the PtO_2 reference. In addition, the EXAFS of h-PtAg-NW exhibits the absence of a characteristic peak associated with Pt−O−Pt (clustered Pt oxides) scatterings at 3.16 Å compared to PtO_2, implying its unique structure rather than typical Pt oxides. The bonding environment for the Pt atoms in h-PtAg-NW is then investigated by least-squares EXAFS curve fitting analysis. Tables S1 and S2 summarize the structural parameters obtained from the EXAFS fitting analysis. After the electrochemical oxidation of PtAg-NW, the coordination number of Pt−Ag significantly decreased from 7.9 to 1.6, as expected due to the dissolution of Ag from intermetallic PtAg. As shown in the Pt L_3-edge XANES spectra (Figure 2j), the white line intensity of the Pt adsorption edge and features of PtAg-NW is notably lower than that of PtO_2 and similar to that of Pt foil, suggesting that Pt predominantly exists in a metallic form in PtAg-NW. On the other hand, the adsorption edge in the signal of h-PtAg-NW shifts slightly toward the positive direction with a higher white line intensity, which is closer to that of PtO_2, indicating an increase in the Pt chemical state and formation of oxidized structure after etching (inset of Figure 2j).[50] The different Pt L_3-edge oscillation amplitudes in the $k^3\chi(k)$ oscillation curves also indicate a local coordination environment change of the Pt sites from PtAg-NW to h-PtAg-NW, with a characteristic difference in the range of 5−6 $Å^{-1}$ (Figure 2k). The wavelet-transformed (WT) EXAFS analysis was conducted as a vivid way to distinguish the backscattering atoms and interaction environment of Pt in PtAg-NW and h-PtAg-NW catalysts. As shown in Figure 2l−n and Figure S11, the WT contour plot of PtAg-NW exhibits only one intensity maximum at approximately 9.5 $Å^{-1}$, assigned to Pt−Ag and Pt−Pt contributions. For h-PtAg-NW, besides the Pt−Pt and Pt−Ag signal at 9.4 $Å^{-1}$, another signal plateau at near 4.8 $Å^{-1}$ is exclusively observed, which is assigned to the appearance of Pt−O contribution in h-PtAg-NW, clearly different from that in PtAg-NW. These XAFS results confirm the occurrence of partial oxidation on the PtAg surface but without forming clustered Pt oxides during the dynamic evolution toward this hollowed nanostructure.

EGOR Performance Evaluation

To evaluate the catalytic performance toward the electrooxidation reaction of EG, the as-synthesized h-PtAg-NW electrocatalyst was initially assessed with a standard three-electrode H-type cell. The linear sweep voltammetry (LSV) polarization curves of h-PtAg-NW, PtAg-NW, Ag-NW, and commercial Pt foil were measured in 1.0 M KOH aqueous solutions with or without 1.5 M EG, respectively (Figure 3a). The currents of h-PtAg-NW and PtAg-NW were drastically increased with the presence of EG, and only an anodic potential of 0.63 V (vs RHE) was needed to reach a current density of 100 mA cm^{-2} on h-PtAg-NW. In contrast, there is only a small oxidation peak at 0.78 V as the oxidation of EG on Pt foil, and no significant oxidation current is observed for Ag-NW until 1.7 V. As shown in Figure 3b, the corresponding Tafel slopes of h-PtAg-NW and PtAg-NW for EGOR are determined to be 108.1 and 102.7 mV/dec, respectively, while the Tafel slopes of Pt foil (248.5 mV/dec) and Ag-NW (189.8 mV/dec) are much higher. At 1.0 V vs RHE, the current density on h-PtAg-NW could reach 355 mA cm^{-2}, surpassing that on PtAg-NW as 224 mA cm^{-2}, demonstrating superior electrocatalytic activity after dynamic evolution. An exceptional mass activity of 16.3 A mg_{Pt}^{-1} at 1.0 V was determined through ICP measurements to quantify the Pt loading on the electrode, which benefited from the high atom-utilization efficiency in the hollowed nanostructure. The electrochemically active surface area (ECSA) was also estimated using the double-layer capacitance (C_{dl}) with h-PtAg-NW measured as 7.72 mF cm^{-2} and 193 cm^{-2}, which approximately doubles that of PtAg-NW (3.57 mF cm^{-2}, 89.2 cm^{-2}), suggesting the exposure of the interior surface area with core dissolution (Figure S12). The ECSA determined by CO stripping measurement ($ECSA_{CO}$) was further calculated and shows that $ECSA_{CO}$ of h-PtAg-NW is approximately doubled in comparison to that of PtAg-NW (Figure S13), which is in accordance with the double-layer capacitance result. Meanwhile, the potential oxygen evolution reaction (OER) on h-PtAg-NW is almost negligible with the presence of EG in the electrolyte, which was also confirmed by the gas chromatography analysis, in which no O_2 was detected in the anodic compartment (Figure S14). The characteristic redox features of h-PtAg-NW and PtAg-NW were further investigated by cyclic voltammetry (CV) measurement (Figure 3c and Figure S15). The appearance of an EG electrooxidation wave was ranging from positive direction of 0.4 to 1.2 V at the EG concentration of 0.05 M, with a significantly higher current on h-PtAg-NW than that on PtAg-NW. The subsequent anodic peaks (from 1.3 to 1.6 V) and corresponding cathodic peaks (from 1.2 to 0.8 V) could be contributed to the redox pair of Pt-related oxides according to literatures.[51−53] These results indicate that the catalytic activity of h-PtAg-NW has a distinctive origin rather than the formation of Pt-related oxides at high potential, and h-PtAg-NW has an advantage on EGOR kinetically compared to unetched PtAg-NW. The open circuit potential (OCP) measurement were further performed to reveal the adsorption and activation feature of the EG molecule at the inner Helmholtz layer (Figure 3d).[54,55] Upon the addition of 0.05 M EG, h-PtAg-NW exhibited the largest OCP decrease with ΔU = 0.73 V and PtAg-NW shows a slightly lower ΔU = 0.68 V, which is much greater than those of Pt foil (Δ = 0.53 V) and Ag-NW (Δ = 0.08 V), indicating that EG has been effectively adsorbed and activated on the inner Helmholtz layer of h-PtAg-NW and PtAg-NW. The OCP response toward glycolate was also investigated and demonstrated that the electrooxidation product glycolate could be more easily desorbed from the h-PtAg-NW surface compared to PtAg-NW (Figure S16). In addition, the reaction charge transfer characteristics were explored by performing electrochemical impedance spectroscopy (EIS) at different external potentials with the presence of EG for h-PtAg-NW and PtAg-NW (Figure S17). The optimum fitting result reveals that h-PtAg-NW delivers a

https://doi.org/10.1021/jacsau.4c00975
JACS Au 2025, 5, 714−726

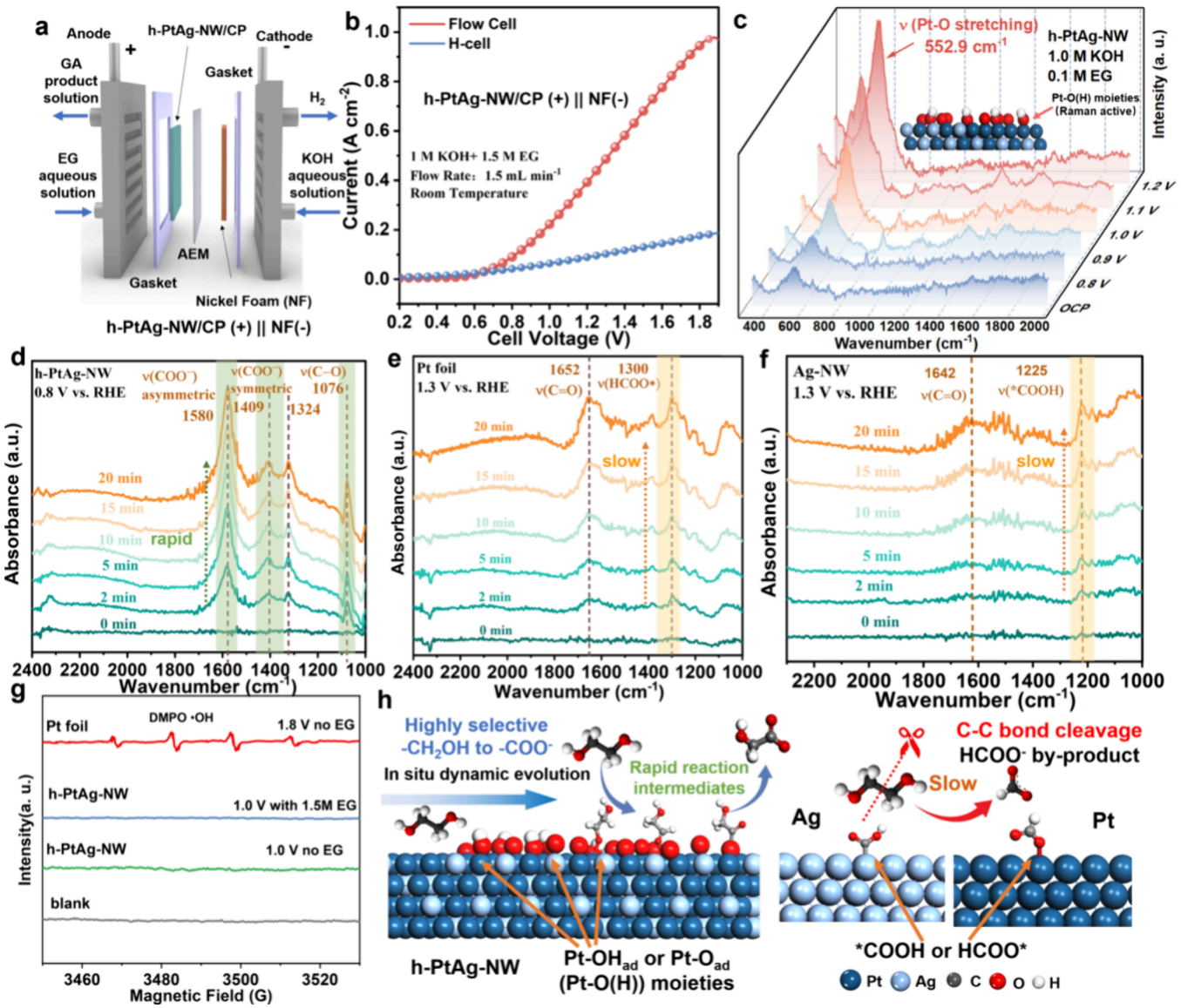

Figure 4. (a) Schematic illustration of AEM flow cell configuration with the h-PtAg-NW catalyst on CP with the NF counter electrode. (b) LSV profiles of h-PtAg-NW with the NF counter electrode in the two-electrode flow cell or H-cell for EGOR (scan rate of 5 mV s^{-1}). (c) In situ Raman spectra of the h-PtAg-NW catalyst within 1.5 M EG and 1.0 M KOH with varied potentials. (d–f) In situ ATR-FTIR spectra of the h-PtAg-NW catalyst Ag-NW and Pt foil reference within 1.5 M EG in 1.0 M KOH. The dashed line labels the representative signal emergence with the reaction proceeding. (g) EPR spectra of the h-PtAg-NW and Pt foil reference with applied potentials in 1.0 M KOH electrolyte, using DMPO as a trapping agent. (h) Schematic drawing of the reaction pathways, the influence of surficial oxidation and Pt–O(H) moieties on h-PtAg-NW, and the C–C dissociation on the Pt or Ag surface.

smaller interfacial charge transfer resistance (R_{ct}) in comparison to PtAg-NW with EG, which rationalizes the high EGOR electrocatalytic activity through rapid charge transfer kinetics during the reaction.

To identify the reaction selectivity, chronoamperometry (CA) measurements were carried out, where the products were quantitatively analyzed by high-performance liquid chromatography (HPLC) with the linear fitting of standard concentrations (Figures S15 and S19). After sustained reaction for 1 h in 1.0 M KOH electrolyte with 1.5 M EG, an excellent EGOR performance is obtained for h-PtAg-NW with the average selectivity of glycolate of 98% and the faradic efficiency (FE) of 97% ranging from 0.6 to 1.4 V (Figure 3e). The highest FE of 98.3% is acquired at 1.0 V vs RHE with a current density of ca. 340 mA cm^{-2}, which is selected as the optimal potential. The results of ^{1}H NMR demonstrate that glycolate is the primary product, while a negligible quantity of formate was detected (Figure S20). The glycolate selectivity of 99.2% of h-PtAg-NW at 1.0 V vs RHE is significantly superior to those of commercial Pt/C (51.2%) and Ag-NW (36.7%), while unetched PtAg-NW exhibits a slightly lower glycolate selectivity of 91.3% than that of h-PtAg-NW (Figure 3f). To further identify the optimal conditions for the electrooxidation of EG, we also varied the concentrations of KOH and EG and measured the product selectivity of glycolate on the h-PtAg-NW catalyst in these conditions at 1.0 V vs RHE. The 1.5 M EG and 1.0 M KOH are screened out as the optimal condition while variation in concentrations of either OH^- or EG could contribute to a reduction in glycolate selectivity. (Figure S21). The performance of the controlled samples of Pt_xAg-NW was also evaluated

https://doi.org/10.1021/jacsau.4c00975
JACS Au 2025, 5, 714–726

through the same protocol. The formation of hollow nanostructures was observed exclusively with $Pt_{0.5}$Ag-NW and PtAg-NW precursors attributed to the optimized Pt loading, and the highest EGOR performance was achieved with h-PtAg-NW (Figures S22 and S23). To demonstrate the stability and practicability of h-PtAg-NW in EGOR, CA measurements were carried out with 1.0 V vs RHE for 4 h, resulting in an oxidative current of ca. 320 mA cm^{-2} achieved in the system (Figure S24). The products were collected every 20 min and analyzed by online HPLC. Surprisingly, as the target product, the selectivity of glycolate remains above 98% and the FE exceeds more than 96% even after the reaction for 3 h despite the constant increase of glycolate concentrations in the system (Figure 3g,h). Over extended periods of operation, particularly after 3 h, a gradual decrease in current density was observed, potentially attributed to the adsorption of contaminating species or the formation of PtO_x on the catalytic surface. However, a rapid restoration could be easily achieved through the activation CV scan at the beginning of the catalytic cycle. Therefore, we measured the performance and product through six activation cycles with a total period of 12 h at 0.8 V vs RHE, achieving both >98% selectivity and >96% FEs and a current density of ∼250 mA cm^{-2} in every cycle (Figure 3i and Figure S25). The TEM images and XPS spectra of h-PtAg-NW were also characterized with no significant change after long-term operation (Figure S26). A pulsed electrolysis strategy was also employed and evaluated with h-PtAg-NW in order to prevent the deactivation phenomenon, exhibiting great current stability and selectivity of glycolate >98% (Figure S27).[56] The excellent current density, selectivity, and overpotential observed for h-PtAg-NW outperform the majority of metal or metal oxide catalysts and are comparable to the foremost Pd- or Au-based system for EG to glycolate electrooxidation in H-type cell configuration[5,57] (Figure 3j, Figure S28, and Table S3). In order to further evaluate the industrial feasibility of h-PtAg-NW and EGOR in an electrolyzer system, we assembled a flow cell with an anion exchange membrane (AEM) with h-PtAg-NW deposited on CP as the anode and nickel foam (NF) as the cathode for the hydrogen evolution reaction (HER) (Figure 4a). As demonstrated by the catalytic performance, the LSV curves (Figure 4b) show that the electrooxidation of EG to glycolate reaches an industrially related current of 412 mA cm^{-2} at a cell voltage of 1.2 V and 945 mA cm^{-2} (24.1 A mg_{Pt}^{-1}) at 1.8 V in this AEM flow cell configuration, which is much higher than that in the corresponding two-electrode H-cell with the same anode and cathode, revealing the outstanding potential of h-PtAg-NW in an AEM-based electrolyzer for industrial EGOR application. We also probed the EG oxidation product through the CA measurements with activation cycles in the flow cell electrolyzer, resulting in the FE and selectivity of glycolate as 95.2 and 96.9% along with hydrogen production, respectively (Figures S29 and S30), which is consistent with those in the three-electrode H-cell system.

Mechanistic Elucidation

To further gain the mechanism information and rationalize the catalytic performance of the h-PtAg-NW catalyst for the selective electrooxidation of EG to glycolate, in situ Raman spectroscopy and attenuated total reflectance Fourier transform infrared spectroscopy (ATR-FTIR) characterization was performed to elucidate the reaction intermediates of EGOR at applied positive potential (Figure S31). Figure 4c illustrates the potential-dependent in situ Raman spectroscopy of h-PtAg-NW acquired in 1.5 M EG and 1.0 M KOH electrolytes with 100 mV increments. As the external potentials elevated from the OCP and 0.8 to 1.2 V, a significant appearance of Raman peak was detected at 552.9 cm^{-1} on h-PtAg-NW. This signal is notably indicative of the Pt−O stretching vibration mode associated with the potential Pt−OH_{ad} and Pt−O_{ad} (denoted as Pt−O(H)) moieties generated during glycolate formation, which also intensified as the potential moved positively.[58,59] Note that the potential range of 0.8−1.2 V is prior to the oxidation peak of Pt oxide generation in CV measurement, which implies that the in situ formation Pt−O(H) moieties on h-PtAg-NW are distinctive from typical PtO_x oxides. This behavior stands in contrast to the control experiment in which no Pt−O bond or other intermediates' Raman signal was detected with Pt foil and/or Ag-NW in the same operando condition (Figure S32). The emergence of Pt−O(H)-related moieties appears to be strongly associated with the highly selective electrooxidation of a single hydroxyl group in EG. Moreover, the ATR-FTIR spectra were recorded in 1.0 M KOH electrolyte with the presence of 1.5 M EG at 1.30 V vs RHE. The electrocatalyst was applied onto the ATR silicon wafer with microstructure for signal enhancement. By excluding the background of the system at the OCP, the variation of the IR signal originating from the electrochemical reaction intermediates was successfully detected. As shown in Figure 4d, the rapid appearance of a series of peaks at 1580, 1409, 1324, and 1076 cm^{-1} at 0.8 V (vs RHE) on h-PtAg-NW could be attributed to the characteristic absorption of asymmetric and symmetric stretching modes from the COO^- and $-CH_2OH$ segments in the glycolate anion (Figure S33), which was further enhanced over an extended time with a positive potential applied. No other significant intermediates could be traced, and the progressive enhancement of these peaks corroborates the increased adsorption and concentration of product glycolate as the reaction proceeded, highlighting the rapid kinetics of this electrochemical reaction and high selectivity on the h-PtAg-NW catalyst. To better unveil the mechanistic insight behind the difference between glycolate and formate's selectivity, we therefore included Ag nanowires and Pt foil as the control reference in the in situ FTIR measurements, upon which formate was observed as the major byproduct during electrooxidation. As shown in Figure 4e and 4f, two distinct peak pairs of 1300, 1652 and 1225, 1642 cm^{-1} slowly emerged even at a high potential of 1.3 V (vs RHE) with Pt foil and Ag nanowires, respectively. The relatively slow rate of signal intensification implies the sluggish kinetics of intermediate formation and accumulation. The signals at 1644 and 1652 cm^{-1} could be ascribed as a typical asymmetric C═O stretching mode in the carboxyl group. In addition, the 1225 and 1300 cm^{-1} peaks are in agreement with the OH deformation of a *COOH intermediate bound to Ag and symmetric O−C−O stretching modes of bonded HCOO* on Pt, respectively, signifying the different configurations of C1 adsorption.[60−63] Given the high proportion of formate product in both Ag NWs and Pt foil, the *COOH or HCOO* species formed seem to be key intermediates associated with the C−C bond breakage and thus the $HCOO^-$ generation on the Ag or Pt surface. It is noteworthy that no detectable EPR signal could be observed when using 5,5-dimethyl-1-pyrroline-1-oxide (DMPO) as a radical trapping agent at 1.0 V versus RHE on h-PtAg-NW despite a high EGOR current density, suggesting that the EGOR to glycolate on h-PtAg-NW is not primarily

https://doi.org/10.1021/jacsau.4c00975
JACS Au 2025, 5, 714−726

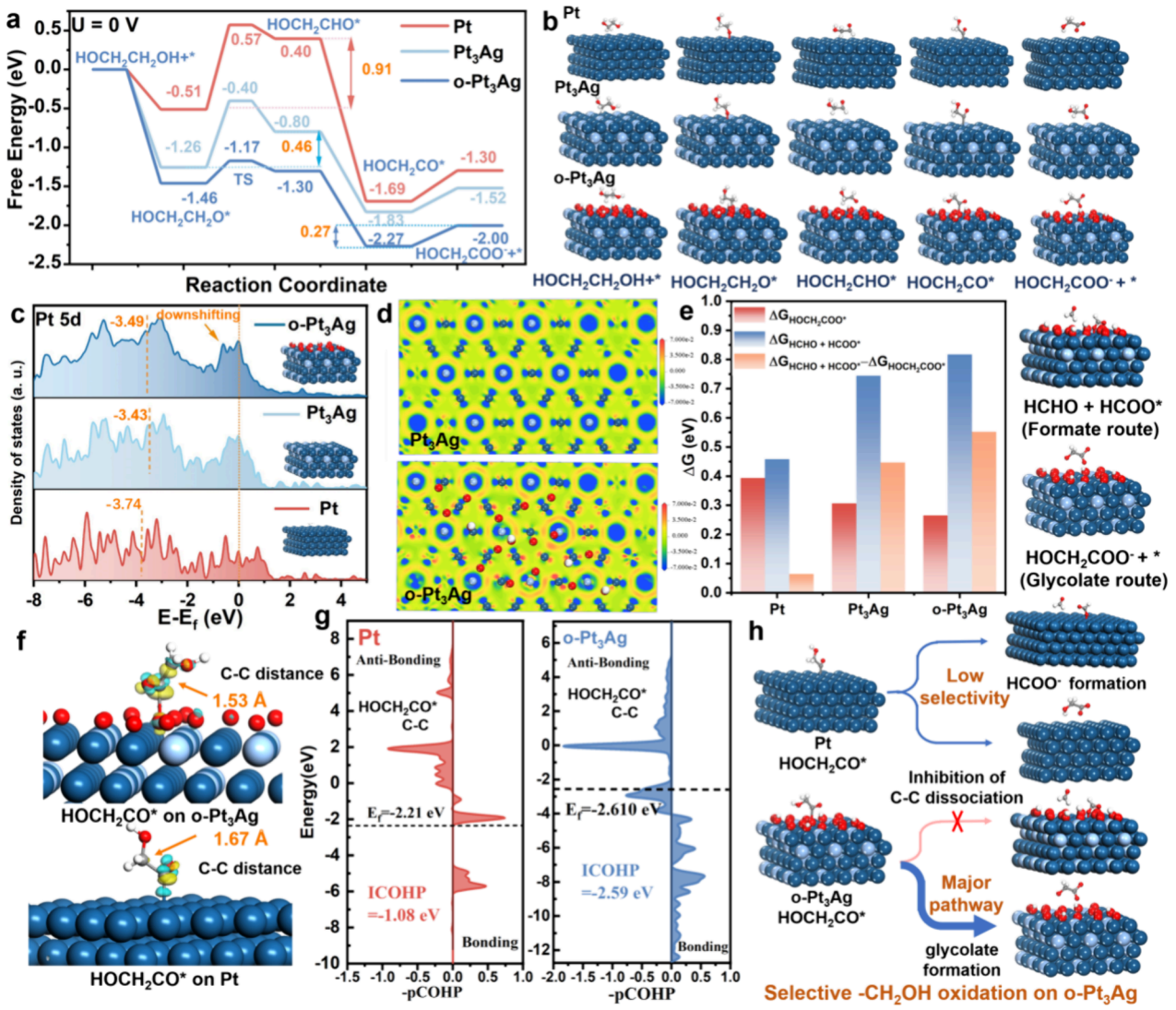

Figure 5. (a) Free energy diagram of the EGOR on the Pt(111), Pt_3Ag, and *o*-Pt_3Ag surfaces based on DFT calculation as well as the corresponding optimized structure (b) for the energy step (blue: Pt; cyan: Ag; red: O). (c) Density of states of the 5d orbit in Pt and Pt_3Ag and *o*-Pt_3Ag, with the d-band center and downshifting near the E_f labeled. (d) Deformation charge density of the PtAg and *o*-Pt_3Ag surfaces. Red and blue regions indicate positive charge accumulation and depletion, respectively. (e) Free energy comparison of the $HOCH_2CO^*$ to $HOCH_2COO^-$ ($\Delta G_{HOCH2CO^*}$) or C−C dissociation pathway HCOO* + HCHO ($\Delta G_{HCHO+HCOO^*}$) on Pt, Pt_3Ag, and *o*-Pt_3Ag surfaces. (f) Differential charge density upon adsorption of the $HOCH_2CO^*$ intermediate on *o*-Pt_3Ag (top) and Pt (bottom), with C−C distances labeled. Cyan and yellow isosurfaces represent electron charge depletion and accumulation, respectively. (g) COHP of the C−C bond in $HOCH_2CO^*$ adsorbed on the Pt and *o*-Pt_3Ag surfaces with ICOHP calculated. (h) Schematic drawing of the difference of reaction pathway selectivity on Pt and *o*-Pt_3Ag.

mediated by anodic •OH radicals (Figure 4g). On the basis of the above results, we speculated that the C−C bond dissociation is strongly inhibited over the h-PtAg-NW catalyst with the in situ formed surficial Pt−O(H) moieties on the PtAg nanostructure, leading to a rapid reaction pathway from EG to glycolate. Meanwhile, the formation of C1 intermediates from the C−C bond cleavage of EG on metallic Pt and Ag results in low selectivity and formate pathway in EGOR (Figure 4h).

We further performed DFT calculations to rationalize the operando results and validate the outstanding electrooxidation selectivity of glycolate on the h-PtAg-NW surface instead of pure Pt. Given the electrocatalytic process of EGOR with glycolate as the desired product, a stepwise four PCET pathway was proposed in the DFT investigation, along with the reaction intermediates of $HOCH_2CH_2O^*$, $HOCH_2CHO^*$, $HOCH_2CO^*$, and $HOCH_2COO^*$ species considered. Based on XAFS and in situ Raman characterization, the appearance of the Pt−O(H) signal suggests that the mild surficial oxidation of the PtAg alloy likely occurred during the preparation of h-PtAg-NW's hollowed nanostructure and also the electro-oxidation reaction. Accordingly, our investigation centers on the Pt (111) surface, the representative Pt_3Ag alloy (111) surface, and a model structure with oxygen atoms and hydroxyl atop the Pt_3Ag (111) surface (*o*-Pt_3Ag) (Figure S34). The Gibbs free-energy diagrams calculated with optimized geometries are demonstrated in Figure 5a,b. The *o*-Pt_3Ag and Pt_3Ag surfaces exhibit greater energetic favorability for the initial EG chemisorption compared to the Pt surface. Notably, for the Pt(111) surface, the oxidation of adsorbed hydroxyl $-CH_2O^*$ to aldehyde $-CHO^*$ intermediate possesses the highest free energy changes (ΔG) of 0.91 V, considered as the rate-limiting step. Meanwhile, this reaction pathway is much more readily for Pt_3Ag and *o*-Pt_3Ag surfaces while their ΔG of

https://doi.org/10.1021/jacsau.4c00975
JACS Au 2025, 5, 714−726

the limiting steps were calculated to be 0.46 and 0.27 V, respectively. This significant disparity of reaction energy barrier reveals that the introduction of Ag in composition and the surficial Pt−O(H) groups can modulate the adsorption energy of intermediates in EGOR, consistent with the superior electrocatalytic current exhibited by h-PtAg-NW in contrast to that of Pt foil. In addition, the projected density of states (PDOS) analysis demonstrated a downward shift of Pt 5d states near the Fermi level (E_f) and the d-band center from Pt_3Ag (−3.43 eV) to *o*-Pt_3Ag (−3.49 eV) (Figure 5c and Figure S36). According to the d-band center theory, this downshifting of the d-band could facilitate the desorption of $HOCH_2CO$* intermediates, thereby enhancing the reaction kinetics and thus the oxidation current.[64] Moreover, the deformation charge density shows that there are increased positive charge distributions on the *o*-Pt_3Ag surface after the introduction of electronegative −OH and −O moieties compared to that of Pt_3Ag, which generates a local electrophilic region on *o*-Pt_3Ag for the potential adsorption of alcohols (Figure 5d and Figure S37). Furthermore, this result is consistent with the more negative EG adsorption ΔG in the first step of the EGOR pathway on *o*-Pt_3Ag (−1.46 eV for *o*-Pt_3Ag, −1.26 eV for Pt_3Ag, and −0.51 eV for Pt), indicating a higher likelihood and efficiency for the adsorption and activation of EG on bimetallic PtAg with the surficial oxidation. The transition state (TS) of the $HOCH_2CH_2O$* to $HOCH_2CHO$* steps on the Pt(111), Pt_3Ag, and *o*-Pt_3Ag surfaces was further calculated, with the lowest activation energy (0.29 eV) found on the *o*-Pt_3Ag surface (Figure S35). As indicated by in situ FTIR results, we also investigated the energy perspective of the competitive C−C dissociation route on the catalytic surface, which is strongly correlated with high $HCOO^-$ byproduct yield and the HCOO* intermediate experimentally observed on Pt foil. As illustrated in Figure 5e and Figure S38, the difference in ΔG between the step of $HOCH_2CO$* to $HOCH_2COO^-$ ($\Delta G_{HOCH2CO*}$) and the step of $HOCH_2CO$* to HCOO* and HCHO ($\Delta G_{HCHO+HCOO*}$) through oxidative C−C cleavage is compared for Pt, Pt_3Ag, and *o*-Pt_3Ag. In this pathway-determining step, the *o*-Pt_3Ag surface exhibits a $HOCH_2COO^-$ preferred energy with the highest ΔG difference of 0.56 eV, whereas Pt and Pt_3Ag possess lower ΔG differences of 0.07 and 0.48 eV, respectively. From the thermodynamic trends, the minimal ΔG disparity of 0.07 eV between the two pathways on the Pt surface could deteriorate the selectivity of EGOR with a greater tendency of following the C−C dissociation pathway. This result indicates a significantly higher energy barrier for oxidative C−C cleavage on the surface of h-PtAg-NW with the oxidized Pt_3Ag surface in comparison to Pt foil, also rationalizing almost no formate production on h-PtAg-NW and the appearance of the HCOO* signal on Pt foil in the operando FTIR. To further elucidate the electronic structure of the $HOCH_2CO$* intermediate and C−C dissociation mechanism, we performed the Bader charge distribution analysis. Figure 5f and Figure S39 depict the differential charge density distribution of $HOCH_2CO$* on the *o*-Pt_3Ag and Pt (111) surfaces. Intriguingly, the C−C bond of $HOCH_2CO$* with the adsorption on *o*-Pt_3Ag is allocated with a yellow isosurface, representing the accumulation of electron density in the bonding orbit. This augmented electron density signifies an enhancement of the C−C bond within the $HOCH_2CO$ intermediate on *o*-Pt_3Ag. The $HOCH_2CO$* on *o*-Pt_3Ag exhibits a C−C distance of 1.53 Å, which is shorter than the 1.67 Å observed on the Pt(111) surface, thereby reducing the propensity for bond dissociation in the electrocatalytic process. The crystal orbital Hamilton population (COHP) of the C−C bond in $HOCH_2CO$* adsorbed on the Pt and *o*-Pt_3Ag surfaces was further calculated in Figure 5g. The integrated COHP (ICOHP) serves as a quantitative descriptor of the strength of the C−C bond. A relatively more positive ICOHP (−1.08 eV) of C−C in $HOCH_2CO$* on Pt indicates a substantially weakened C−C bond on pristine Pt (111) compared to that on *o*-Pt_3Ag (−2.59 eV). These theoretical modeling results successfully corroborate the empirical observations of enhanced selectivity and rapid reaction kinetics with the presence of a mildly oxidized PtAg catalytic surface in the h-PtAg-NW catalyst for the oriented oxidation of the $-CH_2OH$ group in EG, inhibiting the C−C cleavage pathway toward $HCOO^-$ (Figure 5h).

CONCLUSIONS

In conclusion, we have demonstrated a new dynamic electrochemical strategy to synthesize a hollow metallic PtAg alloy nanostructure. Such nanostructure shows an excellent selectivity (up to 99.2%) for the electrooxidation of the hydroxyl group in EG to the carboxyl group given the product glycolate, achieving a current density of ∼350 mA cm^{-2} and an FE around 97% at a potential of 1.0 V vs RHE. An industrial-level current up to 1.0 A cm^{-2} was achieved coupled with hydrogen production in an AEM flow cell assembly with excellent selectivity and low cell voltage. The structural characterization and electrochemical measurements suggested that the shell of the hollowed nanostructure consists of bimetallic PtAg alloy with in situ surficial oxidation and Pt−O(H) moiety formation, which intrinsically enhance the EGOR performance, especially the selectivity. The combination of in situ Raman, FTIR, and DFT analyses further revealed that in contrast to the metallic Pt or Ag surface, the C−C bond dissociation of EG and corresponding C1 intermediates toward formate generation is well suppressed on this hollowed PtAg nanostructure. The rapid reaction kinetics of EGOR to glycolate is achieved with the presence of $Pt-OH_{ad}$ and $Pt-O_{ad}$ moieties. This mild surficial oxidation could modulate the electronic structure and the free energy of adsorbed intermediates, thus facilitating the electrooxidation pathway toward glycolate. This research offers insightful views on designing selective and efficient Pt-based electrocatalysts for selective EGOR toward glycolate. Furthermore, our study illuminates the possibility of fine-tuning the electrochemical performance through in situ dynamic structure and surface adjustments, paving the way for developing hollowed nanostructures and electrocatalysts.

METHODS

Materials

EG, benzyl alcohol (BA), cyclohexane, glycolic acid (GA), formic acid (FA), ethanol absolute, nitric acid (HNO_3), sulfuric acid (H_2SO_4), oleylamine (OAm), oleic acid (OA), potassium hydroxide (KOH), silver nitrate ($AgNO_3$), iron chloride hexahydrate ($FeCl_3·6H_2O$), platinum(ii) acetylacetonate ($Pt(acac)_2$), platinum nanoparticle on carbon (Pt/C, 20%), and polyvinylpyrrolidone (PVP, MW: 40,000) were purchased from Sigma-Aldrich. Ultrapure water (18.2 MΩ/cm) was used for all experimental processes.

Synthesis of Ag Nanowires (Ag-NW)

Silver nanowires were synthesized on the basis of a previously reported hydrothermal method. First, 15 mL of EG was added to the Teflon lining. Then, 250 mg of $AgNO_3$, 400 mg of PVP, and 3.5 g of

https://doi.org/10.1021/jacsau.4c00975
JACS Au 2025, 5, 714−726

the prepared $FeCl_3$-EG solution (0.6 mM) were added to the EG solution and stirred for half an hour at room temperature. After being heated at 140 °C for 5 h, the mixtures were cooled to room temperature and washed with ethanol three times. Ag-NW collected were dispersed in 45 mL of ethanol. 5 mL of concentrated nitric acid was added into 45 mL of the ethanol solution of the Ag-NW. This solution was stirred for 12 h at room temperature and then washed with ethanol three times. The collected product was dissolved in 20 mL of BA solution for subsequent use.

Synthesis of PtAg-NW

A 10 mg portion of $Pt(acac)_2$ was dispersed in a mixture of 8 mL of OAm and 4 mL of OA as a precursor solution. 10 mL of Ag-NW dissolved in BA solution was injected into a flask and stirred for 10 min at 200 °C. The precursor solution was dropwise added at a rate of 3 mL/10 min into the flask. After the drip, the flask was heated at 200 °C for an extra 30 min and finally rapidly cooled to room temperature. The mixture was washed with ethanol and cyclohexane for three times and collected by centrifugation. This production with an actual Pt loading of 3 wt % was dried at 60 °C for 12 h in a vacuum oven. Ag-NW loaded with other Pt mass fractions were similarly prepared and denoted as Pt_xAg-NW, where x represents the relative ratio of $Pt(acac)_2$ loading compared to that of PtAg-NW.

Electrochemical In Situ Dynamic Etching for h-PtAg-NW and Measurements

Electrochemical measurements in the H-cell were performed in a three-electrode system at the CHI 760 electrochemical workstation. A Nafion 117 or Fumasep (FAB-PK-130) membrane was inserted between the cathodic chamber and the anodic chamber. Pt foil and Ag/AgCl (saturated KCl-filled) electrodes were used as the counter electrode and reference electrode, respectively. In a typical preparation of the working electrode, a catalyst ink was prepared by dispersing 4 mg of catalyst, and 40 μL of 5 wt % Nafion solution into 1 mL of 1:1 (v/v) water/ethanol with 1 h sonication bath, and the catalyst ink was loaded and dried into the carbon fiber electrode with catalyst loading of ∼2.0 mg cm^{-2} and doubled for flow cell measurement.

In order to prepare h-PtAg-NW, the carbon fiber electrode with precatalyst PtAg-NW was electrochemically oxidized at 1.40 V vs RHE for 90 min in Ar-saturated 1.0 M KOH and 1.5 M EG aqueous solution. The electrochemical etching and core dissolution of PtAg-NW to h-PtAg-NW then occurred and were characterized. For the partial etching of PtAg-NW, a 30 min electrooxidation treatment was applied. LSV was recorded in N_2-saturated 1.0 M KOH and 1.5 M EG electrolyte at a scan of 5 mV s^{-1} without iR-compensation unless specified. CA measurements were performed via applying a constant potential on the working electrode. The selectivity measurement was generally performed with 1 h electrolysis with constant potential on the catalyst, following the HPLC quantification. The CV was performed at a scan of 20 mV s^{-1} ranging from 0.4 to 1.6 V. The pulsed potential measurement was performed with potential switch between high potential (E_H = 1.0 V_{RHE}, 0.2 s) and low potential (E_L = 0.2 V_{RHE}, 0.5s). The OCP on the working electrode was measured before and after the addition of EG or GA in the three-electrode system. The flow cell measurement was performed with 1 cm^2 electrodes with the two-electrode system and using the Fumasep membrane (FAB-PK-130) as AEM. The electrolyte (1 M KOH + 1.5 M EG) flow rate was controlled at 1.5 mL min^{-1}. The electrode spacing between the counter electrode and working electrode is about 2.5 cm for the flow cell and 5 cm for the H-cell. The electrochemical double-layer capacitance (C_{dl}) was calculated by a series of CV curves at various scan rates in the non-faradic region. All potentials were converted to the reversible hydrogen electrode (RHE) scale by E (vs RHE) = E (vs Ag/AgCl) + 0.197 V + 0.059 × pH.

■ ASSOCIATED CONTENT

Supporting Information

The Supporting Information is available free of charge at https://pubs.acs.org/doi/10.1021/jacsau.4c00975.

Experimental and calculation details, including SEM images, TEM images, EDS mapping, XPS and XRD spectrum, EPR spectra, WT transformation of EXAF, electrochemical capacitance measurements, EIS measurement, ^{1}H NMR, chronoamperometry measurement, in-situ characterizations, and DFT calculations (PDF)

■ AUTHOR INFORMATION

Corresponding Authors

Chenhao Zhang − *Shanghai Key Laboratory of Rare Earth Functional Materials and Education Ministry Key Laboratory of Resource Chemistry, Shanghai Normal University, Shanghai 200234, P. R. China;* orcid.org/0009-0004-6307-1268; Email: chenhao.zhang@shnu.edu.cn

Hui Li − *Shanghai Key Laboratory of Rare Earth Functional Materials and Education Ministry Key Laboratory of Resource Chemistry, Shanghai Normal University, Shanghai 200234, P. R. China;* orcid.org/0000-0001-5058-4751; Email: lihui@shnu.edu.cn

Authors

Yuhan Li − *Shanghai Key Laboratory of Rare Earth Functional Materials and Education Ministry Key Laboratory of Resource Chemistry, Shanghai Normal University, Shanghai 200234, P. R. China*

Qingliang Liao − *Shanghai Key Laboratory of Rare Earth Functional Materials and Education Ministry Key Laboratory of Resource Chemistry, Shanghai Normal University, Shanghai 200234, P. R. China*

Peiyi Ji − *Shanghai Key Laboratory of Rare Earth Functional Materials and Education Ministry Key Laboratory of Resource Chemistry, Shanghai Normal University, Shanghai 200234, P. R. China*

Sheng Jie − *Shanghai Key Laboratory of Rare Earth Functional Materials and Education Ministry Key Laboratory of Resource Chemistry, Shanghai Normal University, Shanghai 200234, P. R. China*

Chunjie Wu − *Shanghai Key Laboratory of Rare Earth Functional Materials and Education Ministry Key Laboratory of Resource Chemistry, Shanghai Normal University, Shanghai 200234, P. R. China*

Kunyi Tong − *Shanghai Key Laboratory of Rare Earth Functional Materials and Education Ministry Key Laboratory of Resource Chemistry, Shanghai Normal University, Shanghai 200234, P. R. China*

Minghui Zhu − *State Key Laboratory of Chemical Engineering, East China University of Science and Technology, Shanghai 200237, China;* orcid.org/0000-0003-1593-9320

Complete contact information is available at: https://pubs.acs.org/10.1021/jacsau.4c00975

Author Contributions

Y.L., Q.L., and C.Z. designed the research. Y.L. and Q.L. performed the synthesis, electrochemical experiments, and corresponding analysis. P.J. and J.S. contributed to EXAFS analysis. Y.L. and C.Z. conducted the theorectical analysis. Y.L., C.W., K.T., and M.Z. performed and supervised the operando characterizations. M.Z., C.Z., and H.L. supervised the research. All authors discussed the experimental data and wrote the manuscript. CRediT: **Yuhan Li** data curation, formal

https://doi.org/10.1021/jacsau.4c00975
JACS Au 2025, 5, 714−726

analysis, investigation, software, validation, visualization, writing - original draft; **Qingliang Liao** data curation, investigation; **Peiyi Ji** formal analysis; **Sheng Jie** data curation, formal analysis, methodology; **Chunjie Wu** data curation, formal analysis, visualization; **Kunyi Tong** investigation, validation, visualization; **Minghui Zhu** investigation, resources, supervision; **Chenhao Zhang** conceptualization, data curation, formal analysis, funding acquisition, investigation, project administration, resources, software, supervision, writing - review & editing.

Notes

The authors declare no competing financial interest.

■ ACKNOWLEDGMENTS

This work was supported by the National Natural Science Foundation of China (52371140 and 21972093), the Shanghai Frontiers Science Center of Biomimetic Catalysis, and the Shanghai Engineering Research Center of Green Energy Chemical Engineering. This work was also supported by the Program for Eastern Young Scholars at Shanghai Institutions and Energy Science and Technology discipline under the Shanghai Class IV Peak Disciplinary Development Program.

■ REFERENCES

(1) Wang, F.; Stahl, S. S. Electrochemical Oxidation of Organic Molecules at Lower Overpotential: Accessing Broader Functional Group Compatibility with Electron−Proton Transfer Mediators. *Acc. Chem. Res.* **2020**, *53* (3), 561−574.

(2) Shi, S.-H.; Liang, Y.; Jiao, N. Electrochemical Oxidation Induced Selective C−C Bond Cleavage. *Chem. Rev.* **2021**, *121* (1), 485−505.

(3) Garcia, A. C.; Kolb, M. J.; van Nierop y Sanchez, C.; Vos, J.; Birdja, Y. Y.; Kwon, Y.; Tremiliosi-Filho, G.; Koper, M. T. M. Strong Impact of Platinum Surface Structure on Primary and Secondary Alcohol Oxidation during Electro-Oxidation of Glycerol. *ACS Catal.* **2016**, *6* (7), 4491−4500.

(4) Ye, F.; Zhang, S.; Cheng, Q.; Long, Y.; Liu, D.; Paul, R.; Fang, Y.; Su, Y.; Qu, L.; Dai, L.; Hu, C. The role of oxygen-vacancy in bifunctional indium oxyhydroxide catalysts for electrochemical coupling of biomass valorization with CO2 conversion. *Nat. Commun.* **2023**, *14* (1), 2040.

(5) Yan, Y.; Zhou, H.; Xu, S.-M.; Yang, J.; Hao, P.; Cai, X.; Ren, Y.; Xu, M.; Kong, X.; Shao, M.; Li, Z.; Duan, H. Electrocatalytic Upcycling of Biomass and Plastic Wastes to Biodegradable Polymer Monomers and Hydrogen Fuel at High Current Densities. *J. Am. Chem. Soc.* **2023**, *145* (11), 6144−6155.

(6) Taniguchi, I.; Yoshida, S.; Hiraga, K.; Miyamoto, K.; Kimura, Y.; Oda, K. Biodegradation of PET: Current Status and Application Aspects. *ACS Catal.* **2019**, *9* (5), 4089−4105.

(7) Yue, H.; Zhao, Y.; Ma, X.; Gong, J. Ethylene glycol: properties, synthesis, and applications. *Chem. Soc. Rev.* **2012**, *41* (11), 4218−4244.

(8) Joo, S.; Cho, I. J.; Seo, H.; Son, H. F.; Sagong, H. Y.; Shin, T. J.; Choi, S. Y.; Lee, S. Y.; Kim, K. J. Structural insight into molecular mechanism of poly(ethylene terephthalate) degradation. *Nat. Commun.* **2018**, *9* (1), 382.

(9) Samantaray, P. K.; Little, A.; Haddleton, D. M.; McNally, T.; Tan, B.; Sun, Z.; Huang, W.; Ji, Y.; Wan, C. Poly(glycolic acid) (PGA): a versatile building block expanding high performance and sustainable Bioplastic applications. *Green Chem.* **2020**, *22* (13), 4055−4081.

(10) Rittinghaus, R. D.; Zenner, J.; Pich, A.; Kol, M.; Herres-Pawlis, S. Master of Chaos and Order: Opposite Microstructures of PCL-co-PGA-co-PLA Accessible by a Single Catalyst**. *Angew. Chem., Int. Ed.* **2022**, *61* (11), No. e202112853.

(11) Wu, X.; Wang, Y.; Wu, Z.-S. Design principle of electrocatalysts for the electrooxidation of organics. *Chem.* **2022**, *8* (10), 2594−2629.

(12) Wu, J.; Li, J.; Li, Y.; Ma, X.; Zhang, W.; Hao, Y.; Cai, W.; Liu, Z.; Gong, M. Steering the Glycerol Electro-Reforming Selectivity via Cation−Intermediate Interactions. *Angew. Chem., Int. Ed.* **2022**, *61* (11), No. e202113362.

(13) Qiao, B.; Yang, T.; Shi, S.; Jia, N.; Chen, Y.; Chen, X.; An, Z.; Chen, P. Highly Active Hollow RhCu Nanoboxes toward Ethylene Glycol Electrooxidation. *Small* **2021**, *17* (10), No. 2006534.

(14) Xu, Y.; Han, L. Comprehensive understanding of electro-oxidation of ethylene glycol. *Int. J. Hydrogen Energy* **2014**, *39* (14), 7278−7290.

(15) Qin, Y.; Zhang, W.; Wang, F.; Li, J.; Ye, J.; Sheng, X.; Li, C.; Liang, X.; Liu, P.; Wang, X.; Zheng, X.; Ren, Y.; Xu, C.; Zhang, Z. Extraordinary p−d Hybridization Interaction in Heterostructural Pd-PdSe Nanosheets Boosts C−C Bond Cleavage of Ethylene Glycol Electrooxidation. *Angew. Chem., Int. Ed.* **2022**, *61* (16), No. e202200899.

(16) Si, D.; Xiong, B.; Chen, L.; Shi, J. Highly selective and efficient electrocatalytic synthesis of glycolic acid in coupling with hydrogen evolution. *Chem. Catal.* **2021**, *1* (4), 941−955.

(17) Chang, S. C.; Ho, Y.; Weaver, M. J. Applications of real-time FTIR spectroscopy to the elucidation of complex electroorganic pathways: electrooxidation of ethylene glycol on gold, platinum, and nickel in alkaline solution. *J. Am. Chem. Soc.* **1991**, *113* (25), 9506−9513.

(18) Li, Z.; Zhang, Y.; Zou, B.; Wu, Z.; Gao, F.; Du, Y. Simple Synthesis of PdAg Porous Nanowires as Effective Catalysts for Polyol Oxidation Reaction. *Inorg. Chem.* **2022**, *61* (25), 9693−9701.

(19) Li, J.; Li, L.; Ma, X.; Han, X.; Xing, C.; Qi, X.; He, R.; Arbiol, J.; Pan, H.; Zhao, J.; Deng, J.; Zhang, Y.; Yang, Y.; Cabot, A. Selective Ethylene Glycol Oxidation to Formate on Nickel Selenide with Simultaneous Evolution of Hydrogen. *Adv. Sci.* **2023**, *10* (15), No. 2300841.

(20) Li, Z.; Yan, Y.; Xu, S. M.; Zhou, H.; Xu, M.; Ma, L.; Shao, M.; Kong, X.; Wang, B.; Zheng, L.; Duan, H. Alcohols electrooxidation coupled with H2 production at high current densities promoted by a cooperative catalyst. *Nat. Commun.* **2022**, *13* (1), 147.

(21) Ge, Z.-X.; Ding, Y.; Wang, T.-J.; Shi, F.; Jin, P.-J.; Chen, P.; He, B.; Yin, S.-B.; Chen, Y. Interfacial engineering of holey platinum nanotubes for formic acid electrooxidation boosted water splitting. *J. Energy Chem.* **2023**, *77*, 209−216.

(22) Sakong, S.; Groß, A. The Importance of the Electrochemical Environment in the Electro-Oxidation of Methanol on Pt(111). *ACS Catal.* **2016**, *6* (8), 5575−5586.

(23) Lum, Y.; Huang, J. E.; Wang, Z.; Luo, M.; Nam, D.-H.; Leow, W. R.; Chen, B.; Wicks, J.; Li, Y. C.; Wang, Y.; Dinh, C.-T.; Li, J.; Zhuang, T.-T.; Li, F.; Sham, T.-K.; Sinton, D.; Sargent, E. H. Tuning OH binding energy enables selective electrochemical oxidation of ethylene to ethylene glycol. *Nat. Catal.* **2020**, *3* (1), 14−22.

(24) Li, T.; Harrington, D. A. An Overview of Glycerol Electrooxidation Mechanisms on Pt. *Pd and Au. ChemSusChem* **2021**, *14* (6), 1472−1495.

(25) Li, A.-Z.; Yuan, B.-J.; Xu, M.; Wang, Y.; Zhang, C.; Wang, X.; Wang, X.; Li, J.; Zheng, L.; Li, B.-J.; Duan, H. One-Step Electrochemical Ethylene-to-Ethylene Glycol Conversion over a Multitasking Molecular Catalyst. *J. Am. Chem. Soc.* **2024**, *146* (8), 5622−5633.

(26) Xie, C.; Niu, Z.; Kim, D.; Li, M.; Yang, P. Surface and Interface Control in Nanoparticle Catalysis. *Chem. Rev.* **2020**, *120* (2), 1184−1249.

(27) Chen, J.; Zhang, F.; Kuang, M.; Wang, L.; Wang, H.; Li, W.; Yang, J. Unveiling synergy of strain and ligand effects in metallic aerogel for electrocatalytic polyethylene terephthalate upcycling. *Proc. Natl. Acad. Sci. U. S. A.* **2024**, *121* (17), No. e2318853121.

(28) Yang, X.; Yuan, Q.; Sheng, T.; Wang, X. Mesoporous Mo-doped PtBi intermetallic metallene superstructures to enable the complete electrooxidation of ethylene glycol. *Chem. Sci.* **2024**, *15* (12), 4349−4357.

(29) Sun, L.; Lv, H.; Feng, J.; Guselnikova, O.; Wang, Y.; Yamauchi, Y.; Liu, B. Noble-Metal-Based Hollow Mesoporous Nanoparticles:

https://doi.org/10.1021/jacsau.4c00975
JACS Au 2025, 5, 714−726

Synthesis Strategies and Applications. *Adv. Mater.* **2022**, *34* (31), No. 2201954.
(30) Yang, M.; Zhang, C. H.; Li, N. W.; Luan, D.; Yu, L.; Lou, X. W. Design and Synthesis of Hollow Nanostructures for Electrochemical Water Splitting. *Adv. Sci.* **2022**, *9* (9), No. 2105135.
(31) Park, J.; Kwon, T.; Kim, J.; Jin, H.; Kim, H. Y.; Kim, B.; Joo, S. H.; Lee, K. Hollow nanoparticles as emerging electrocatalysts for renewable energy conversion reactions. *Chem. Soc. Rev.* **2018**, *47* (22), 8173−8202.
(32) Wang, L.; Yamauchi, Y. Metallic Nanocages: Synthesis of Bimetallic Pt−Pd Hollow Nanoparticles with Dendritic Shells by Selective Chemical Etching. *J. Am. Chem. Soc.* **2013**, *135* (45), 16762−16765.
(33) Li, Y.; Zhou, W.; Tanriover, I.; Hadibrata, W.; Partridge, B. E.; Lin, H.; Hu, X.; Lee, B.; Liu, J.; Dravid, V. P.; Aydin, K.; Mirkin, C. A. Open-channel metal particle superlattices. *Nature* **2022**, *611* (7937), 695−701.
(34) Ouyang, Y.; Cao, H.; Wu, H.; Wu, D.; Wang, F.; Fan, X.; Yuan, W.; He, M.; Zhang, L. Y.; Li, C. M. Tuning Pt-skinned PtAg nanotubes in nanoscales to efficiently modify electronic structure for boosting performance of methanol electrooxidation. *Appl. Catal. B: Environ.* **2020**, *265*, No. 118606.
(35) Tan, S. F.; Chee, S. W.; Baraissov, Z.; Jin, H.; Tan, T. L.; Mirsaidov, U. Intermediate Structures of Pt−Ni Nanoparticles during Selective Chemical and Electrochemical Etching. *J. Phys. Chem. Lett.* **2019**, *10* (20), 6090−6096.
(36) Du, J.; Quinson, J.; Zhang, D.; Wang, B.; Wiberg, G. K. H.; Pittkowski, R. K.; Schröder, J.; Simonsen, S. B.; Kirkensgaard, J. J. K.; Li, Y.; Reichenberger, S.; Barcikowski, S.; Jensen, K. M. Ø.; Arenz, M. Nanocomposite Concept for Electrochemical In Situ Preparation of Pt−Au Alloy Nanoparticles for Formic Acid Oxidation. *JACS Au* **2022**, *2* (7), 1757−1768.
(37) Zhao, F.; Yuan, Q.; Nie, S.; Wu, L.; Wang, X. Modified electronic structure and enhanced hydroxyl adsorption make quaternary Pt-based nanosheets efficient anode electrocatalysts for formic acid-/alcohol-air fuel cells. *J. Energy Chem.* **2024**, *92*, 142−150.
(38) Kim, H.; Yoo, T. Y.; Bootharaju, M. S.; Kim, J. H.; Chung, D. Y.; Hyeon, T. Noble Metal-Based Multimetallic Nanoparticles for Electrocatalytic Applications. *Adv. Sci.* **2022**, *9* (1), No. 2104054.
(39) Mistry, H.; Varela, A. S.; Kühl, S.; Strasser, P.; Cuenya, B. R. Nanostructured electrocatalysts with tunable activity and selectivity. *Nat. Rev. Mater.* **2016**, *1* (4), 16009.
(40) van der Ham, M. P. J. M.; van Keulen, E.; Koper, M. T. M.; Tashvigh, A. A.; Bitter, J. H. Steering the Selectivity of Electrocatalytic Glucose Oxidation by the Pt Oxidation State. *Angew. Chem., Int. Ed.* **2023**, *62* (33), No. e202306701.
(41) Li, C.; Iqbal, M.; Lin, J.; Luo, X.; Jiang, B.; Malgras, V.; Wu, K. C. W.; Kim, J.; Yamauchi, Y. Electrochemical Deposition: An Advanced Approach for Templated Synthesis of Nanoporous Metal Architectures. *Acc. Chem. Res.* **2018**, *51* (8), 1764−1773.
(42) Liu, X.; Jiang, Y.; Huang, J.; Zhong, W.; He, B.; Jin, P.; Chen, Y. Bifunctional PdPt bimetallenes for formate oxidation-boosted water electrolysis. *Carbon Energy* **2023**, *5* (12), No. e367.
(43) Fidiani, E.; Pravitasari, R. D.; Damisih; Hapsari, A. U.; Budiman, A. H.; Dewi, E. L.; Du, S. Porous PtAg Nanowires: A Highly Active Platinum Loading Electrocatalyst for Oxygen Reduction Reaction in Proton Exchange Membrane Fuel Cells. *ACS Appl. Energy Mater.* **2024**, *7* (2), 556−564.
(44) Parente, M.; van Helvert, M.; Hamans, R. F.; Verbroekken, R.; Sinha, R.; Bieberle-Hütter, A.; Baldi, A. Simple and Fast High-Yield Synthesis of Silver Nanowires. *Nano Lett.* **2020**, *20* (8), 5759−5764.
(45) Sun, Y.; Ren, Y.; Liu, Y.; Wen, J.; Okasinski, J. S.; Miller, D. J. Ambient-stable tetragonal phase in silver nanostructures. *Nat. Commun.* **2012**, *3* (1), 971.
(46) Pan, Y.-T.; Yan, Y.; Shao, Y.-T.; Zuo, J.-M.; Yang, H. Ag−Pt Compositional Intermetallics Made from Alloy Nanoparticles. *Nano Lett.* **2016**, *16* (10), 6599−6603.
(47) Tao, L.; Sun, M.; Zhou, Y.; Luo, M.; Lv, F.; Li, M.; Zhang, Q.; Gu, L.; Huang, B.; Guo, S. A General Synthetic Method for High-Entropy Alloy Subnanometer Ribbons. *J. Am. Chem. Soc.* **2022**, *144* (23), 10582−10590.
(48) Moreau, L. M.; Schurman, C. A.; Kewalramani, S.; Shahjamali, M. M.; Mirkin, C. A.; Bedzyk, M. J. How Ag Nanospheres Are Transformed into AgAu Nanocages. *J. Am. Chem. Soc.* **2017**, *139* (35), 12291−12298.
(49) Cuin, A.; Massabni, A. C.; Leite, C. Q. F.; Sato, D. N.; Neves, A.; Szpoganicz, B.; Silva, M. S.; Bortoluzzi, A. J. Synthesis, X-ray structure and antimycobacterial activity of silver complexes with α-hydroxycarboxylic acids. *J. Inorg. Biochem.* **2007**, *101* (2), 291−296.
(50) Zeng, L.; Zhao, Z.; Huang, Q.; Zhou, C.; Chen, W.; Wang, K.; Li, M.; Lin, F.; Luo, H.; Gu, Y.; Li, L.; Zhang, S.; Lv, F.; Lu, G.; Luo, M.; Guo, S. Single-Atom Cr−N4 Sites with High Oxophilicity Interfaced with Pt Atomic Clusters for Practical Alkaline Hydrogen Evolution Catalysis. *J. Am. Chem. Soc.* **2023**, *145* (39), 21432−21441.
(51) Chung, D. Y.; Lee, K.-J.; Sung, Y.-E. Methanol Electro-Oxidation on the Pt Surface: Revisiting the Cyclic Voltammetry Interpretation. *J. Phys. Chem. C* **2016**, *120* (17), 9028−9035.
(52) John, J.; Wang, H.; Rus, E. D.; Abruña, H. D. Mechanistic Studies of Formate Oxidation on Platinum in Alkaline Medium. *J. Phys. Chem. C* **2012**, *116* (9), 5810−5820.
(53) Vonk, V.; Volkov, S.; Keller, T. F.; Hutterer, A.; Lakner, P.; Bertram, F.; Fleig, J.; Opitz, A. K.; Stierle, A. Reversible Ultrathin PtOx Formation at the Buried Pt/YSZ(111) Interface Studied In Situ under Electrochemical Polarization. *J. Phys. Chem. Lett.* **2023**, *14* (8), 2065−2071.
(54) Zhou, P.; Lv, X.; Tao, S.; Wu, J.; Wang, H.; Wei, X.; Wang, T.; Zhou, B.; Lu, Y.; Frauenheim, T.; Fu, X.; Wang, S.; Zou, Y. Heterogeneous-Interface-Enhanced Adsorption of Organic and Hydroxyl for Biomass Electrooxidation. *Adv. Mater.* **2022**, *34* (42), No. 2204089.
(55) Gattrell, M.; Kirk, D. W. A Study of the Oxidation of Phenol at Platinum and Preoxidized Platinum Surfaces. *J. Electrochem. Soc.* **1993**, *140* (6), 1534.
(56) Chen, W.; Zhang, L.; Xu, L.; He, Y.; Pang, H.; Wang, S.; Zou, Y. Pulse potential mediated selectivity for the electrocatalytic oxidation of glycerol to glyceric acid. *Nat. Commun.* **2024**, *15* (1), 2420.
(57) Shi, K.; Si, D.; Teng, X.; Chen, L.; Shi, J. Pd/NiMoO4/NF electrocatalysts for the efficient and ultra-stable synthesis and electrolyte-assisted extraction of glycolate. *Nat. Commun.* **2024**, *15* (1), 2899.
(58) Kumeda, T.; Kondo, K.; Tanaka, S.; Sakata, O.; Hoshi, N.; Nakamura, M. Surface Extraction Process During Initial Oxidation of Pt(111): Effect of Hydrophilic/Hydrophobic Cations in Alkaline Media. *J. Am. Chem. Soc.* **2024**, *146* (15), 10312−10320.
(59) Sugimura, F.; Sakai, N.; Nakamura, T.; Nakamura, M.; Ikeda, K.; Sakai, T.; Hoshi, N. In situ observation of Pt oxides on the low index planes of Pt using surface enhanced Raman spectroscopy. *Phys. Chem. Chem. Phys.* **2017**, *19* (40), 27570−27579.
(60) Firet, N. J.; Smith, W. A. Probing the Reaction Mechanism of CO2 Electroreduction over Ag Films via Operando Infrared Spectroscopy. *ACS Catal.* **2017**, *7* (1), 606−612.
(61) Zhu, S.; Li, T.; Cai, W.-B.; Shao, M. CO2 Electrochemical Reduction As Probed through Infrared Spectroscopy. *ACS Energy Lett.* **2019**, *4* (3), 682−689.
(62) Gao, D.; Zhou, H.; Cai, F.; Wang, D.; Hu, Y.; Jiang, B.; Cai, W.-B.; Chen, X.; Si, R.; Yang, F.; Miao, S.; Wang, J.; Wang, G.; Bao, X. Switchable CO2 electroreduction via engineering active phases of Pd nanoparticles. *Nano Res.* **2017**, *10* (6), 2181−2191.
(63) McPherson, I. J.; Ash, P. A.; Jacobs, R. M. J.; Vincent, K. A. Formate adsorption on Pt nanoparticles during formic acid electro-oxidation: insights from in situ infrared spectroscopy. *Chem. Commun.* **2016**, *52* (85), 12665−12668.
(64) Chen, S.; Liu, N.; Zhong, J.; Yang, R.; Yan, B.; Gan, L.; Yu, P.; Gui, X.; Yang, H.; Yu, D.; Zeng, Z.; Yang, G. Engineering Support and Distribution of Palladium and Tin on MXene with Modulation of the d-Band Center for CO-resilient Methanol Oxidation. *Angew. Chem., Int. Ed.* **2022**, *61* (45), No. e202209693.

https://doi.org/10.1021/jacsau.4c00975
JACS Au 2025, 5, 714−726